A mixed-mode cohesive-zone model accounting for finite dilation and asperity degradation

Roberto Serpieri*[1], Giulio Alfano[2], Elio Sacco[3]

[1]Dipartimento di Ingegneria, Università degli Studi del Sannio, Piazza Roma, 21 - I. 82100, Benevento, Italy. E-mail: roberto.serpieri@unisannio.it

[2]School of Engineering and Design, Brunel University, Kingston Lane, UB8 3PH, Uxbridge, UK. E-mail: giulio.alfano@brunel.ac.uk

[3]Università di Cassino e del Lazio Meridionale, Dipartimento di Ingegneria Civile e Meccanica, Cassino (FR), Italy. E-mail: sacco@unicas.it

Keywords: Cohesive-zone models; Mixed-mode fracture energy; Damage-friction coupling; Wear; Dilation; Interlocking.

Abstract

A cohesive zone model is formulated to describe the mechanics of initiation and propagation of cracks and the associated asperity degradation and nonlinear dilation along structural interfaces of quasi-brittle materials, such as concrete, rocks and masonry, subjected to monotonic or cyclic loading. Using a two-scale approach, a cohesive-law is determined at each point of a smooth macroscale interface by resolving a problem at the micro-scale for a representative interface area (RIA), where the geometry of the asperities is modelled using three differently inclined microplanes. On each microplane a cohesive-frictional cohesive law is then

*Corresponding author

used. In this paper, the finite depth of the asperities is accounted for by considering the progressive reduction in contact area between each couple of interfacing microplanes for increasing opening (macro-scale) relative-displacement. Furthermore, the rupture of the asperities and associated flattening of the fracture surface is captured by a progressive reduction of the inclination angles of the microplanes in the RIA. Numerical examples are reported to assess the sensitivity of the shear-stress slip curves and of the nonlinear dilation upon the geometry of the asperities in the RIA. Numerical-experimental comparisons are then presented to illustrate the predictive capability of the model in simulating granite rock joints subjected to monotonic and cyclic shear loading and the concrete-bar interaction in a pull-out test.

1 Introduction

Interface models are adopted in many engineering applications to simulate different phenomena involving the de-cohesion and detachment processes. They are used, for instance, to describe the adhesion of joined bodies, the interaction of heterogeneities in composite materials, the opening of cracks for the evolution of potential fracture lines, the response of fractured bodies, the formation of narrow bands characterized by high strain gradients.

Interfaces are used at different scales; they are employed:

- at geological scale, to reproduce tectonic movements [23], by employing techniques such as the X-FEM [37], or to simulate the joint propagation across layer interfaces in sedimentary rocks [10];

- at structural scale, to predict the construction response as masonry buildings or parts of them subjected to fractures due to different reasons in static [16] or dynamic [19] frameworks; to assess the effectiveness of strengthening by application of FRP (fiber reinforced plastic) composites to structural elements [35];

- at the scale of the largest particles in composite materials subjected to damage, to evaluate the overall response in conjunction with homogenization processes, as for instance in the case of masonry [22] or fibrous composite materials [24];

- at the nano-scale, to study the crack growth in layered nano-materials [36].

The nonlinear response of the interfaces is modeled applying the concepts of damage mechanics, contact mechanics, plasticity and viscosity theories.

In the context of cohesive interfaces, damage plays the fundamental role of the internal variable governing the intensity of adhesion among the parts joined by the interface [8]. The unilateral contact becomes important during damage evolution, i.e. during the formation of microcracks along the interface. In particular, when microcracks coalesce into a macrocrack, so that complete separation is possible among the joined parts, very different responses occur at the interface when the interface mouths are open or closed, inducing in the latter case a re-stiffening of the interface.

When damage is complete and the interface mouths are closed, sliding between the surfaces of the interface can occur. Classically, sliding is assumed to be governed by Coulomb's law governed by a friction parameter. A review of interface models considering the coupling between friction, adhesion and damage [4, 21], with a discussion of the most widely used cohesive zone models, has been presented in [20]. A strategy to combine a contact algorithm and a cohesive approach has been also proposed in [30] to model damage in masonry panels driven by interface debonding coupled with frictional contact.

Sliding between interface surfaces can be accompanied by the dilatancy effect, i.e. the presence of relative displacement in the direction normal to the interface. Dilatancy can play a very important role in the overall response of a system including interfaces, as in the case of fractured rocks. The literature concerning the specific issue of modeling ditatancy and its rational derivation from micromechanical approaches is extensive.

In [18] a two scale model is proposed: at macroscopic level a constitutive law appli-

cable to a large class of contact-friction problems is given; then, micro-level asperities are considered, inducing interlocking and dilatancy. The degradation of the asperities is also considered. For interfaces in geomaterials, a model able to consider the dependency of dilatancy on the mean effective pressure was proposed in [5] while, more recently, a micromechanical constitutive model for simulating the behaviour of fully formed cracks in geomaterials accounting for roughness of the crack surface was proposed in [13]. A constitutive law able to satisfactorily reproduce the mechanical response of interfaces subjected to cyclic loading histories can be derived from elasto-plasticity theory. A formulation of a constitutive model for cyclic loading histories leading to the opening, re-closure and sliding accompanied by dilation or contraction was proposed in [31]. The model is based on a micromechanical analysis of the interface considering the presence of sawtooth asperities responsible for the dilatancy. A related numerical procedure was also developed and implemented in a commercial computer code.

The problem of the stability of an assemblage of masonry elements interconnected by dry joints subjected to unilateral contact, friction and dilatancy effects is approached in [17]. It is assumed that the friction angle can be decomposed into two components, one responsible for the dissipative response and one for the dilatancy; an analysis concerning the possible states of equilibrium and displacement is presented. An interface constitutive model accounting for the dilatancy phenomenon was proposed also in [14]. The model is based on a micromechanical kinematic conjecture in which distinction is made between sliding strain and micro-slip strain; in particular, the latter is derived considering spherical asperity interaction with variation of the contact area. A model of an interface with micro-dilatancy was presented in [33], for studying the fiber-matrix degradation of composite materials, based on a micromechanical model which takes into account the role played by the interaction of asperities.

Several interface micromechanical mechanisms have been analyzed in [34], which include damage and de-cohesion evolution, the interaction of primary and secondary asperities, the asperity wear and the formation of a granular layer. Crack propagation in

concrete dams was studied in [3] developing a damage-friction interface model which account also for the possible water pressure effects, the unilateral contact and the dilatancy. The model is derived from a simplified micromechanical scheme. The friction and the dilatancy effects are governed by two different angles and are formulated in a phenomenological context. A thermodynamically consistent interface model, based on damage and plasticity theories applied on the micromechanical idea given in [3], was proposed in [32]. The model is mainly formulated to simulate the mechanical response of the mortar in masonry material. Dilatancy is governed by two angles and is included in a phenomenological way in the framework of a non-associativity rule.

A review of the literature reveals that dilatancy is reproduced developing micromechanical models or, more often, phenomenological approaches. Micromechanics has the advantage of allowing a rational derivation of the phenomenon, but it can require the use of quite simple schemes; on the other hand, phenomenological approaches often can be more easily integrated in finite element codes.

In this paper an interface model is derived from a micromechanical analysis; the model considers de-cohesion, unilateral contact, friction and dilation. The micro-model is characterized by defining a representative interface area (RIA) with sawtooth asperities according to the scheme proposed in [25] and, more recently, discussed in [26].

The model is developed in a two-dimensional context and the RIA is defined with a simplified, yet effective geometry consisting of three microplanes, one horizontal and two inclined of equal and opposite angles, which are responsible for the dilation effect. It is assumed that the three planes have the same area; the interface model given in [4] is adopted for each plane.

Unlike the models in [25, 26], here the finite depth of the asperities is accounted for in the formulation by enforcing equilibrium of the interfacing parts of the RIA in the deformed configuration, so that the progressive reduction of the contact area for an increasing opening displacement is considered.

Furthermore, the progressive reduction of the interlocking effect due to wear of the

asperities and the consequent flattening of the surfaces at the micro-scale is also captured by the model through an exponential reduction of the inclination angle of the microplanes of the RIA.

A sensitivity analysis with respect to the model parameters that represent the geometry of the asperities at the micro-scale is presented to better illustrate the model features. Finally, the predictive capabilities of the model is shown by reporting the results of the numerical simulation of granite rock joints subjected to monotonic and cyclic shear loading, which were experimentally tested by Lee et al. [12], together with the simulation of the pull-out test of a steel bar from a concrete block, which was carried out experimentally by Shima et al. [28], and by comparing numerical results versus experimental ones.

The paper is organized as follows. Section 2 describes the formulation of the model, illustrating the main ideas and model assumptions to account for the finite depth of the asperities and their progressive wear. Details of the implementations are reported in Section 3. Section 4 reports the numerical results, starting from those of the sensitivity analyses and, then, illustrating the model validation comparing the numerical results with the experimental data obtained in [12, 28]. Finally, conclusions are drawn in Section 5.

2 Model formulation

The main ideas and related key equations behind the model that is proposed are presented in this section.

Two-dimensional problems will be considered in which, within a body occupying a domain Ω, an interface Γ is pre-defined, where a crack can initiate and propagate. Accordingly, on Γ the displacement field is allowed to be discontinuous.

Following [25] and [26], the main features of the present formulation are:

- A two-scale approach is used: at the macro-scale the interface is assumed to be

smooth, and indeed without loss of generality problems where Γ is a straight line (Figure 1(a)) are considered; at the micro-scale, the actual geometry of the asperities of the fracture surface is accounted for (Figure 1(b)).

- The macro-scale problem is solved numerically using a finite-element (FE) formulation, with interface elements placed along Γ, and an appropriate nonlinear solution scheme. The above assumption means that the details of the asperities do not have to be captured by the spatial FE discretization.

- At the micro-scale the geometry of the asperities is simplified by assuming a periodic pattern (Figure 1(c)), with a repeating unit made of a finite number N_p of straight microplanes, that will be referred to as the representative interface area (RIA). In the applications considered in this paper $N_p = 3$ and the RIA shown in Figure 1(d) is chosen. Furthermore, the asperities are assumed infinitely stiff and all the deformation of the interface within the RIA is defined by a unique relative-displacement vector $\mathbf{s}$. In this way, on each microplane k the macro-scale relative displacement $\mathbf{s}$ is decomposed into mode-I and mode-II components depending on the inclination angle θ_k of the microplane, and the corresponding local mode-I and mode-II stress components are computed accounting for elastic damage and friction using the model developed by Alfano and Sacco in [4].

- To link the two scales, at each integration point of each interface element of the macro-scale model the cohesive law, which relates the relative displacement vector $\mathbf{s}$ to the interface stress $\boldsymbol{\sigma}$, is determined by resolving the microscale problem for the RIA.

- In order to use, on each microplane, an associated-type damage evolution law with the use of a single damage variable in a neater and thermodynamically consistent way, the same fracture energy in modes I and II are employed [26].

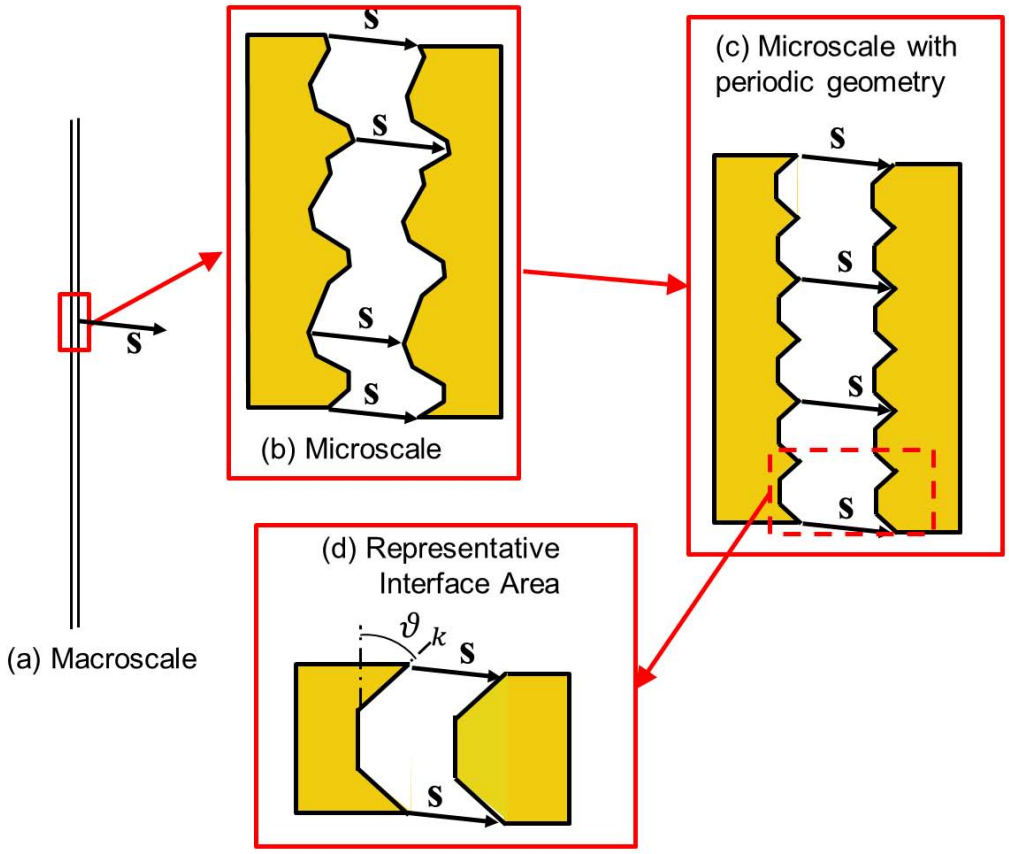

Figure 1: Multiscale scheme: (a) flat macro-scale geometry; (b) geometry of the asperities accounted for at the micro-scale; (c) micro-scale geometry with simplified periodic pattern; (d) representative interface area (repeating unit).

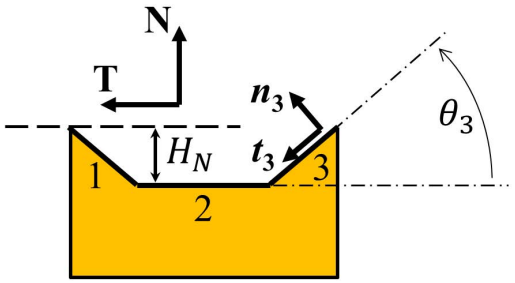

Figure 2: Details of the RIA showing the microplane numbers, 1,2 and 3, the local ($\{\mathbf{n}_k, \mathbf{t}_k\}$) and global ($\{\mathbf{N}, \mathbf{T}\}$) reference systems, the depth H_N of the asperities and the inclination angles the θ_k of microplanes.

- At the macro-scale, the increase in fracture energy which is typically measured for increasing mode-II/mode-I ratio is retrieved thanks to the interaction between interlocking and friction captured by the multi-scale model.

The novel enhancements herein proposed are:

- The finite depth of the asperities is accounted for by taking into account the progressive reduction in contact area between each couple of interfacing microplanes for increasing opening (macro-scale) relative-displacement (see Figure 3), up to a point when the latter is larger than the assumed asperities depth, H, at which point no interface stress is transmitted.

- The progressive degradation of the interlocking effect, due to the rupture of the asperities and associated flattening of the fracture surface is captured by a progressive reduction of the inclination angles of the microplanes in the RIA.

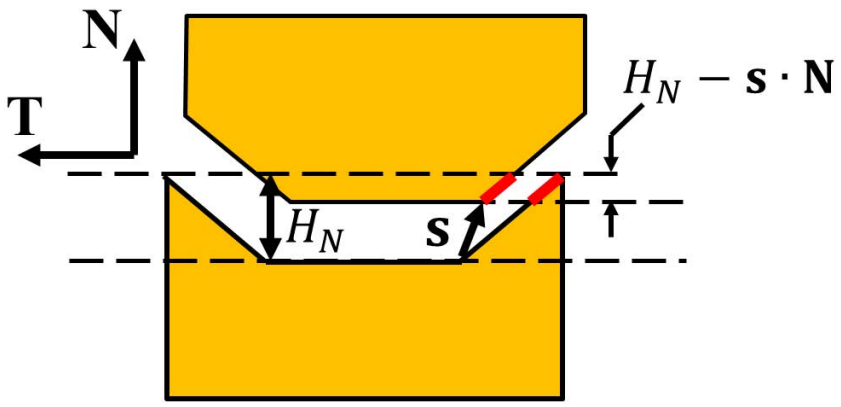

Figure 3: Reduction in contact area along inclined microplanes depending on the opening displacement $s_N = \mathbf{s} \cdot \mathbf{N}$.

In the following subsection the essential features of the model proposed in [25] and [26] are recalled. Subsequently, in Subsections 2.2 and 2.3 the two above mentioned enhancements of the model are described in more detail.

2.1 Interlocking interface model

The free energy per unit area Ψ is defined as the weighted sum of the free energies associated with each microplane [25]:

$$\Psi = \sum_{k=1}^{N_p} \gamma_k \Psi_k \tag{1}$$

where Ψ_k is the free energy per unit area of the $k-$th microplane, γ_k is its weight coefficient, and N_p is the number of microplanes. Coefficient γ_k can be related to the 'area fractions' of the k-th inclined plane, which are defined as follows. Denoting by A_P the overall area of the RIA, by A_k the effective area of the k-th microplane, and by $A = \sum_{k=1}^{N_p} A_k$ the total area of all microplanes, the following relations hold

$$\gamma_k = \frac{A_k}{A_P} = \hat{\gamma}_k \frac{A}{A_P} \tag{2}$$

where $\hat{\gamma}_k = \dfrac{A_k}{A}$ is the effective area fraction of the k-th plane. Notice that, denoting by A_{Pk} the area of the projection of A_k onto the average interface plane, $A_P = \sum_{k=1}^{N_p} A_{Pk}$. By definition of $\hat{\gamma}_k$, one has $\sum_{k=1}^{Np} \hat{\gamma}_k = 1$.

The macroscopic stress turns out to be expressed as the weighted sum of the contribution of each microplane

$$\boldsymbol{\sigma} = \frac{\partial \Psi}{\partial \mathbf{s}} = \sum_{k=1}^{N_p} \gamma_k \, \boldsymbol{\sigma}_k \qquad \text{where } \boldsymbol{\sigma}_k = \frac{\partial \Psi_k}{\partial \mathbf{s}} \tag{3}$$

2.1.1 Microplane constitutive law

The (specific) free energy on each microplane, Ψ_k, is written as follows:

$$\Psi_k(D_k, \mathbf{s}, s_{kf}) = \frac{1}{2}\,(1 - D_k)\,(K_n\, s_{kn}^2 + K_t\, s_{kt}^2) + \frac{1}{2}\, D_k \;\left[K_n\, \langle s_{kn} \rangle_-^2 + K_t\,(s_{kt} - s_{kf})^2\right] \tag{4}$$

where s_{kn} and s_{kt} are the relative-displacement components in (local) modes I and II, i.e. the components with respect to the local microplane reference system, K_n and K_t are the elastic stiffnesses in modes I and II, s_{kf} denotes the inelastic frictional slip on the damaged part of the microplane while $\langle x \rangle_-$ denotes the negative part of x. In agreement with most of the cohesive-zone models proposed in the literature, K_n and K_t are introduced in the form of penalty stiffness factors that must be not too high to avoid ill-conditioning, yet sufficiently high to correctly capture the behavior of the undamaged interface [2].

The local relative-displacement components s_{kn} and s_{kt} are related to the global ones, s_N and s_T through a rotation matrix $\mathbf{R}_k$:

$$\begin{bmatrix} s_{kn} \\ \\ s_{kt} \end{bmatrix} = \begin{bmatrix} \cos\theta_k & \sin\theta_k \\ \\ -\sin\theta_k & \cos\theta_k \end{bmatrix} \begin{bmatrix} s_N \\ \\ s_T \end{bmatrix} = \mathbf{R}_k \begin{bmatrix} s_N \\ \\ s_T \end{bmatrix} \tag{5}$$

Differentiation of the local microplane free energy provides the local stress components:

$$\begin{bmatrix} \sigma_{kn} \\ \\ \sigma_{kt} \end{bmatrix} = (1 - D_k) \begin{bmatrix} K_n \, s_{kn} \\ \\ K_t \, s_{kt} \end{bmatrix} + D_k \begin{bmatrix} K_n \, \langle s_{kn} \rangle_- \\ \\ K_t \, (s_{kt} - s_{kf}) \end{bmatrix} \tag{6}$$

Using a Coulomb-like friction law the frictional slip s_{kf} on each microplane is the solution to the following problem:

$$\begin{cases} \phi_k(s_{kn}, s_{kt}, s_{kf}) = \mu \, K_n \, \langle s_{kn} \rangle_+ + |K_t \, (s_{kt} - s_{kf})| \\ \\ \dot{s}_{kf} = \dot{\lambda}_k \, \text{sign} \, (s_{kt} - s_{kf}) \\ \\ \dot{\lambda}_k > 0 \qquad \phi_k(s_{kn}, s_{kt}, s_{kf}) \leq 0 \qquad \dot{\lambda}_k \, \phi_k(s_{kn}, s_{kt}, s_{kf}) = 0 \end{cases} \tag{7}$$

2.1.2 Damage evolution law

Damage evolution on each microplane is based on the law defined by Alfano and Crisfield [2], which is in turn based on the bilinear relationships in pure modes I and II, shown in Figure 4. In these relations s_{0n} and s_{0t} denote the damage-initiation relative

displacements in modes I and II, respectively, while s_{cn} and s_{ct} denote the relative-displacement values at which cohesion is lost. Given the peak stresses in modes I and II, σ_{0n} and σ_{0t}, these are related to the s_{cn} and s_{ct} and to the fracture energies in modes I and II, G_{cn} and G_{ct}, by:

$$G_{cn} = \frac{1}{2}\,\sigma_{0n}\,s_{cn} \qquad G_{ct} = \frac{1}{2}\,\sigma_{0t}\,s_{ct} \tag{8}$$

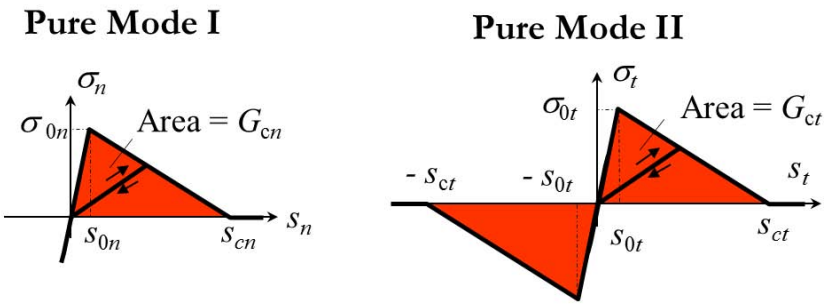

Figure 4: Bilinear laws in pure modes I and II [2].

However, unlike the original model [2], here we build on the recent developments presented by Serpieri et al. [26], where it is shown that to have an associated type of damage evolution law, defined in terms of an equivalent relative displacement, the fracture energies G_{cn} and G_{ct} need to be taken equal, so that the subscripts c and t can be omitted. More importantly, the assumption of a mode-independent value of the fracture energy is supported by a valid physical argument: the fracture energies G_{cn} and G_{ct} only represent here the energy dissipation due to the rupture of bonds. Instead the increase in the total (measured) fracture energy with increasing mode II/mode I ratio is retrieved because of the interlocking effect and the associated additional dissipation due to friction on the inclined planes. For the same reason, as also shown in [26], a unique 'ductility parameter' η for mode I and mode II has to be used:

$$\eta = 1 - \frac{s_{0n}}{s_{cn}} = 1 - \frac{s_{0t}}{s_{ct}} \tag{9}$$

The damage evolution is then given by the following law:

$$D_k = \max\left\{0, \min\left\{1, \frac{\beta_k}{\eta\,(1-\beta_k)}\right\}\right\} \tag{10}$$

where

$$\beta_k = \max_{history} \sqrt{\left(\frac{\langle s_{kn}\rangle_+}{s_{0n}}\right)^2 + \left(\frac{s_{kt}}{s_{0t}}\right)^2} \tag{11}$$

Remark 2.1 It is worth noting that the above physical argument also implies that other types of dissipation, e.g. due to plasticity, viscoelasticity, viscoplasticity, crack branching, are neglected here. This seems a reasonable assumption for the applications studied in Section 4. In different cases, these further types of dissipation can be dealt with by introducing additional internal variables and choosing appropriate evolution laws for them, see e.g. [15] where such approach is used to develop a rate-dependent cohesive model to simulate crack growth along viscoelastic interfaces. ■

Notice that, from equations (8) and (9) (see also Figure 4), it results:

$$K_n = \frac{\sigma_{0n}}{s_{0n}} = \frac{\sigma_{0n}^2}{2\,(1-\eta)\,G_c} = \frac{2G_c}{(1-\eta)\,s_{cn}^2} \tag{12}$$

and

$$K_t = \frac{\sigma_{0t}}{s_{0t}} = \frac{\sigma_{0t}^2}{2\,(1-\eta)\,G_c} = \frac{2G_c}{(1-\eta)\,s_{ct}^2}. \tag{13}$$

When (1), (2) and (4) are combined and K_n and K_t are expressed in terms of (12) and (13), the resulting expression of the free energy is:

$$\begin{aligned}\Psi = \textstyle\sum_{k=1}^{N_p} \hat{\gamma}_k \dfrac{A}{A_P}\dfrac{G_c}{(1-\eta)} \Bigg\{ & (1-D_k)\left[\left(\frac{s_{kn}}{s_{cn}}\right)^2 + \left(\frac{s_{kt}}{s_{ct}}\right)^2\right] \\ & + D_k\left[\left(\frac{\langle s_{kn}\rangle_-}{s_{cn}}\right)^2 + \left(\frac{s_{kt}-s_{kf}}{s_{ct}}\right)^2\right]\Bigg\}\end{aligned} \tag{14}$$

2.2 Modelling of the finite depth of asperities

The finite depth of asperities is accounted for following a rationale which is in several respects similar to the extension of a structural model from infinitesimal displacements to finite displacements: equilibrium is described no longer referring to the initial geometry of the mechanical system, rather referring to its current displaced configuration which, with reference to a given point of the interface, is determined by the displacement vector $\mathbf{s}$.

In particular, with reference to the specific RIA used here, depicted in Figure 2, the main idea is that, for the inclined microplane k (with $\theta_k \neq 0$), the area in potential contact in the deformed configuration is given by (see Figure 3):

$$A_k = \left\langle \frac{H_N - \langle \mathbf{s}\cdot\mathbf{n}\rangle_+}{\sin\theta_k} \right\rangle_+ = \left\langle \frac{H_N - \langle s_N\rangle_+}{\sin\theta_k} \right\rangle_+ = A_{0k} \left\langle 1 - \left\langle \frac{s_N}{H_N} \right\rangle_+ \right\rangle_+ \tag{15}$$

where H_N is the tooth height and A_{0k} is the initial microplane area given by:

$$A_{0k} = \frac{H}{\sin\theta_k} \tag{16}$$

Substituting the expression (15) of the current contact area of plane k into equation (2), the microplane area fraction is now given by:

$$\gamma_k = \frac{A_{0k}}{A_P} \left\langle 1 - \left\langle \frac{s_N}{H_N} \right\rangle_+ \right\rangle_+ = \gamma_{0k}\, \mathcal{A}_g \left(\frac{s_N}{H_N} \right) \tag{17}$$

where γ_{0k} is the initial microplane area fraction whereas $\mathcal{A}_g$ is given by:

$$\mathcal{A}_g(x) = \langle 1 - \langle x\rangle\rangle \tag{18}$$

and controls the geometrical contact decay.

Remark 2.2 Notice that, denoting by $\bar{G}_c$ the macroscopic fracture energy per unit projected interface area, parameters $\hat{\gamma}_{0k}$ and $\bar{G}_c$ constitute an alternative, yet completely

equivalent, set of material parameters which can be conveniently employed in place of parameters γ_{0k} and G_c. Actually, in the light of the energy balance $A_P\bar{G}_c = \sum_{k=1}^{N_p} A_{0k}G_c$ the macroscale and microscale fracture energy densities are related by:

$$\bar{G}_c = \sum_{k=1}^{N_p} \frac{A_{0k}}{A_P} G_c = \sum_{k=1}^{N_p} \gamma_{0k} G_c = \frac{A_0}{A_P} G_c \tag{19}$$

In view of (19) and (2) the following multiplying coefficients are equivalent and can be interchanged in (14):

$$\gamma_{0k} G_c = \hat{\gamma}_{0k} \frac{A_0}{A_P} G_c = \hat{\gamma}_{0k} \bar{G}_c \tag{20}$$

In particular, when parameters $\hat{\gamma}_{0k}$ and $\bar{G}_c$ are employed to specify the RIA material properties, the overall expression of the free energy accounting for the finite depth of asperities (obtained combining (14) with (17) and (20)) turns out to be:

$$\begin{aligned} \Psi = \sum_{k=1}^{N_p} \frac{\hat{\gamma}_{0k}\bar{G}_c}{(1-\eta)} \mathcal{A}_g \left(\frac{s_N}{H_N}\right) \Bigg\{ (1-D_k) \left[\left(\frac{s_{kn}}{s_{cn}}\right)^2 + \left(\frac{s_{kt}}{s_{ct}}\right)^2 \right] \\ + D_k \left[\left(\frac{\langle s_{kn} \rangle_-}{s_{cn}}\right)^2 + \left(\frac{s_{kt} - s_{kf}}{s_{ct}}\right)^2 \right] \Bigg\} \end{aligned} \tag{21}$$

Use of expression (21) is convenient when the overall macroscale fracture energy density $\bar{G}_c$ is among the known data and the microplane distribution and inclination has to be deduced from the macroscopic dilation behavior of the interface.

2.3 Modelling of progressive interlocking degradation

Degradation of asperities is an important structural feature which is added to the interface model in order to capture damage-induced decrease of the interlocking effect [9]. High precision laser profilometer measurements of the surface topography of fractured rock surfaces provide evidence that the geometry of cracked surfaces consists of a multiplicity of asperities whose dimension ranges from macroscopic to microscopic scale, and a strong correlation exists between the observation length-scale and the microplane

inclination [12]. This nature of the asperity distribution would more properly require a statistical treatment [6, 7] . However, in the present work, to retain the deterministic nature of the approach set forth in [4, 25] and keep the number of employed history variables limited, a rationale similar to the one considered in [12] is followed.

Hence, progressive interlocking decrease originated in a microplane k due to asperity degradation is addressed by the following exponential law:

$$\theta_k = (\theta_{k0} - \theta_{kf})\, e^{-\frac{\zeta_k}{\zeta_{k0}}} + \theta_{kf} \tag{22}$$

which relates the current value of the microplane inclination angle θ_k to the frictional work spent in sliding along the local tangential direction of the k-th plane since the beginning of the analysis:

$$\zeta_k = \int_{history} \sigma_{kt}\, ds_{kf} \tag{23}$$

The quantities θ_{k0}, θ_{kf} and ζ_{k0} are parameters defining the evolution of degradation associated with the k-th microplane. In particular θ_{k0} is the microplane inclination angle at the beginning of the analysis, θ_{kf} is its value asymptotically approached when ζ_k tends to infinity whereas ζ_{k0} is a characteristic energy value that controls the rate of degradation.

The effect of changes of θ_k due to interlocking degradation is a variation of the rotation matrix relating the global frame and the local frame of plane k, while variations of area fractions induced by change in θ_k are neglected in the current formulation and coefficients $\hat{\gamma}_{0k}$ are kept as constant parameters.

3 Numerical implementation

The interface model has been implemented in a finite-step time integration scheme following a procedure similar to the one adopted in [25]. While we refer the reader to these

articles for the related details, here we focus on the differences, which are due to the fact that the inclination angle and the area fraction here are not constant in time.

In particular, a time step from time t to time $t + \Delta t$ is considered and the discrete counterpart of (3) is given by:

$$\boldsymbol{\sigma}_{t+\Delta t} = \sum_{k=1}^{N_p} \gamma_{k,t+\Delta t}\, \boldsymbol{\sigma}_{k,t+\Delta t} \tag{24}$$

Since the model is used as constitutive law of interface elements within a conventional, displacement-based nonlinear finite-element analysis, the interface constitutive problem is relative-displacement driven. Hence, at each iteration of the generic increment from time t to time $t + \Delta t$, trial nodal displacements result on each interface point in (assigned) tentative relative displacements $\mathbf{s}_{t+\Delta t}$.

From the assigned values of $\mathbf{s}_{t+\Delta t}$, the new values for the area fractions γ_k are computed. With these values and with the inclination angles θ_k fixed at the value at beginning of the step, the solution algorithm presented in [25] is used. The updated value $\zeta_{k,t+\Delta t}$ of ζ_k is then numerically computed as follows:

$$\zeta_{k,t+\Delta t} = \zeta_{k,t} + \sigma_{kt,t}\,(s_{kf,t+\Delta t} - s_{kf,t}) \tag{25}$$

The tangent algorithmic interface stiffness $\mathbf{K}_t$ is obtained by differentiating Equation (24) with respect to the assigned relative displacement $\mathbf{s}_{t+\Delta t}$:

$$\mathbf{K}_t = \frac{\partial \boldsymbol{\sigma}}{\partial \mathbf{s}} = \sum_{k=1}^{N_p} \left(\boldsymbol{\sigma}_k \otimes \frac{\partial \gamma_k}{\partial \mathbf{s}} + \gamma_k \frac{\partial \boldsymbol{\sigma}_k}{\partial \mathbf{s}} \right) \tag{26}$$

where are quantities are evaluated at time $t + \Delta t$.

The vector term $\dfrac{\partial \gamma_k}{\partial \mathbf{s}}$, which does not appear in [25] where the area fractions are constant in time, is given by:

$$\frac{\partial \gamma_k}{\partial \mathbf{s}} = \gamma_{0k} \frac{\partial \mathcal{A}_g}{\partial x} \frac{\partial x}{\partial \mathbf{s}}, \qquad \text{with } x = \frac{s_N}{H_N} \tag{27}$$

where, on account of (18) and of the above expression of x:

$$\frac{\partial \mathcal{A}_g}{\partial x} = \begin{cases} 1 & \text{if } x \in [0,\, 1] \\ 0 & \text{if } x \notin [0,\, 1] \end{cases} \qquad \text{and} \qquad \frac{\partial x}{\partial \mathbf{s}} = \frac{1}{H_N} \begin{bmatrix} 1 \\ \\ 0 \end{bmatrix}. \tag{28}$$

To evaluate the second term in the sum on the right-hand side of (26), let us first notice that in Equations (24) and (26), the components of $\boldsymbol{\sigma}_k$ are to be evaluated in the global reference system $\{\mathbf{N}, \mathbf{T}\}$, so it becomes:

$$\boldsymbol{\sigma}_k = \begin{bmatrix} \sigma_{kN} \\ \\ \sigma_{kT} \end{bmatrix} = \begin{bmatrix} \cos\theta_k & -\sin\theta_k \\ \\ \sin\theta_k & \cos\theta_k \end{bmatrix} \begin{bmatrix} \sigma_{kn} \\ \\ \sigma_{kt} \end{bmatrix} = \mathbf{R}_k^T \begin{bmatrix} \sigma_{kn} \\ \\ \sigma_{kt} \end{bmatrix} \tag{29}$$

where $\mathbf{R}_k^T$ is the transpose of the rotation matrix in Equation (5). Differentiating one has:

$$\frac{\partial \boldsymbol{\sigma}_k}{\partial \mathbf{s}} = \frac{\partial \mathbf{R}_k^T}{\partial \mathbf{s}} \begin{bmatrix} \sigma_{kn} \\ \\ \sigma_{kt} \end{bmatrix} + \mathbf{R}_k^T \frac{\partial}{\partial \mathbf{s}} \begin{bmatrix} \sigma_{kn} \\ \\ \sigma_{kt} \end{bmatrix} \tag{30}$$

The second term on the right-hand side is evaluated as in [25]. The first term, which does not appear in [25] where the microplane inclinations are constant in time, is a third-order tensor which is evaluated as follows:

$$\frac{\partial \mathbf{R}_k^T}{\partial \mathbf{s}} = \frac{\partial \mathbf{R}_k^T}{\partial \theta_k} \frac{\partial \theta_k}{\partial \zeta_k} \otimes \frac{\partial \zeta_k}{\partial \mathbf{s}} \tag{31}$$

The first factor on the right-hand side is given by:

$$\begin{aligned} \frac{\partial \mathbf{R}_k^T}{\partial \theta_k} &= \frac{\partial}{\partial \theta_k} \begin{bmatrix} \cos\theta_k & -\sin\theta_k \\ \\ \sin\theta_k & \cos\theta_k \end{bmatrix} = \begin{bmatrix} -\sin\theta_k & -\cos\theta_k \\ \\ \cos\theta_k & -\sin\theta_k \end{bmatrix} = \\ &= \begin{bmatrix} 0 & -1 \\ \\ 1 & 0 \end{bmatrix} \begin{bmatrix} \cos\theta_k & -\sin\theta_k \\ \\ \sin\theta_k & \cos\theta_k \end{bmatrix} = \mathbf{R}_{\frac{\pi}{2}}^T \mathbf{R}_k^T \end{aligned} \tag{32}$$

where $\mathbf{R}_{\frac{\pi}{2}}^T$ is the transposed rotation matrix evaluated for $\theta_k = \pi/2$.

The second factor in Equation (31) is obtained by differentiating (22):

$$\frac{\partial \theta_k}{\partial \zeta_k} = -\frac{\theta_{k0} - \theta_{kf}}{\zeta_{k0}} \, e^{-\frac{\zeta_k}{\zeta_{k0}}} \tag{33}$$

The third factor in Equation (31) is given by:

$$\frac{\partial \zeta_k}{\partial \mathbf{s}} = \frac{\partial \zeta_k}{\partial s_{kt}} \frac{\partial s_{kt}}{\partial \mathbf{s}} \tag{34}$$

where, from Equation (23) one has:

$$\frac{\partial \zeta_k}{\partial s_{kt}} = \sigma_{kT} \tag{35}$$

while (5) yields

$$\frac{\partial s_{kt}}{\partial \mathbf{s}} = \begin{bmatrix} -\sin\theta_k \\ \\ \cos\theta_k \end{bmatrix} \tag{36}$$

4 Numerical examples

The results of two sets of numerical examples are reported in this section.

Section 4.1 presents an assessment of the single point response of the proposed interface model, including a sensitivity analysis with respect to parameters H_N, θ_0, θ_f and ζ_0 and a model validation against the experimental results in [12] for pre-cracked granite rock joints under monotonic and cyclic loading.

Section 4.2 then describes the nonlinear finite-element simulation of a pull out test of a ribbed steel bar from a concrete cylinder, in which the proposed model has been used as constitutive law for interface elements. For this application the model has been calibrated and validated against the experimental results reported in [28].

The 2D RIA used is shown in Figure 1. The initial area fractions of the three microplanes are all equal, so that $\hat{\gamma}_{0k} = 1/3$ for all $k = 1, 2, 3$. The moduli of the initial angle of the inclined microplanes have the same absolute value θ_0, so that $-\theta_{01} = \theta_{03} =$

θ_0. Likewise, the final inclination angle that would be asymptotically reached on an inclined microplane in case of full degradation is the same, being $-\theta_{f1} = \theta_{f3} = \theta_f$. However, during damage evolution, the initial symmetry of the RIE is generally lost because degradation evolves independently on each microplane according to Equation (23), so that in general $-\theta_1 \neq \theta_3$. The intermediate microplane has a constant zero inclination so that $\theta_2 = \theta_{02} = \theta_{f2} = 0$.

4.1 Assessment of single point response

In all the sensitivity analyses the response of the interface model is evaluated in terms of shear stress-slip and dilation-slip curves obtained when the slip, s_T, is prescribed to monotonically increase in presence of a constant normal compressive (i.e., negative) stress σ_N.

4.1.1 Sensitivity to H_N

Firstly we focus on the effect of the geometry of the asperities in absence of asperity-related damage, so that the absolute values of the asperity angles remains fixed and equal to $\theta = \theta_0 = \theta_f$. In this case ζ_0 has obviously no effect.

Figures 5 and 6 show the results for $\theta = 45°$ and $\theta = 25°$. Each graph is generated by sweeping parameter H_N from 1 mm to 0.01 mm, while the normal stress is kept constantly equal to $\sigma_N = -0.2$ MPa, and all remaining constitutive interface parameters are set equal to those employed in [25], reported in Table 1. Parameters of Table 1 also define the initial stiffness coefficients K_n and K_t according to relations (12) and (13).

σ_{0n} [MPa]	σ_{0t} [MPa]	$\bar{G}_c$ [KJ/m^2]	η [–]	μ [–]
3.0	3.0	0.3	0.9	0.5

Table 1: Material parameters employed in sensitivity analyses to H_N.

The dilation slip curves, Figures 5(b) and 6(b) , show that dilation attains a finite value with an horizontal asymptote positioned below the threshold value set by H_N.

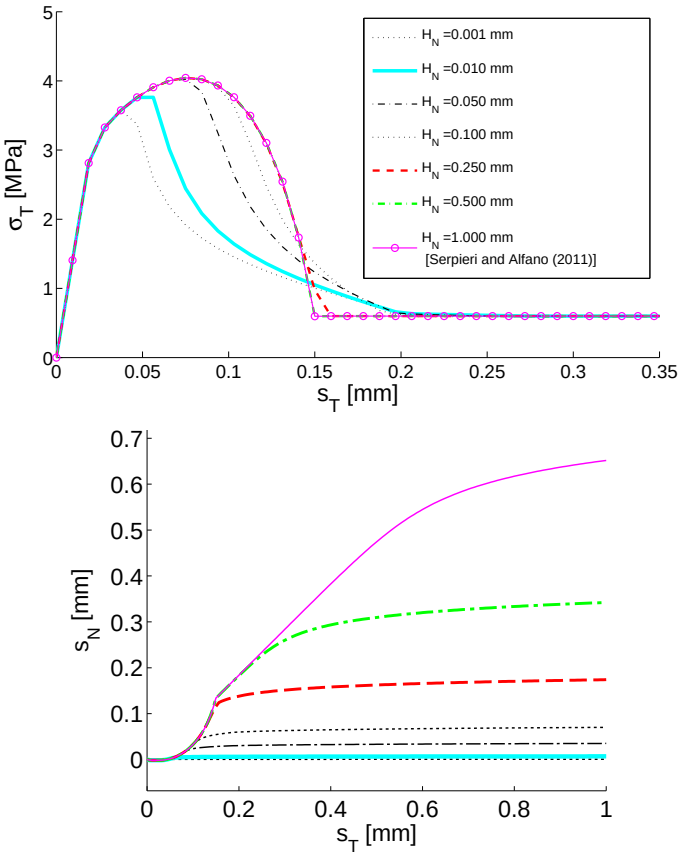

Figure 5: Response obtained for monotonically increasing slip, constant $\sigma_N = -0.2$ MPa and fixed $\theta = 45°$, under different H_N values: (a) shear stress vs. slip ($\sigma_T - s_T$); (b) dilation vs. slip ($s_N - s_T$).

As remarked in the related legends, Figures 5(a), 6(a) show that when H_N is sufficiently high, as expected, the present model recovers the same slip vs. shear stress response of the infinite dilation model reported in [25], which corresponds to $H_N = \infty$. Notice, in particular that the curves in Figures 5(a) and 6(a) for H_N = 0.5 mm and H_N = 1.0 mm already overlap.

An increasingly concave softening branch is obtained as H_N decreases with a lower overall fracture energy. It can be observed that in Figure 5 the softening branch approaches a vertical tangent as H_N tends to zero. Numerical instabilities for extremely low values of H_N were detected. The implemented code cannot handle a zero value of H_N since H_N appears at the denominator of some of the implemented formulas. With

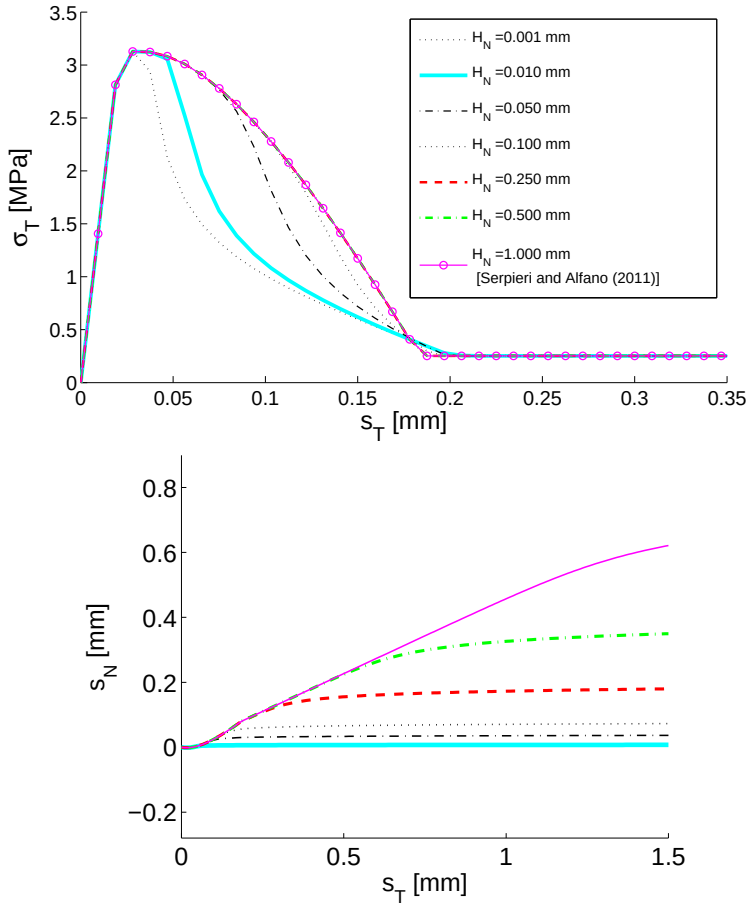

Figure 6: Response obtained for monotonically increasing slip, constant $\sigma_N = -0.2$ MPa and fixed $\theta = 25°$, under different H_N values: (a) shear stress vs. slip ($\sigma_T - s_T$); (b) dilation vs. slip ($s_N - s_T$).

the current formulation and implementation an ideally flat surface has to be reproduced by setting the interlocking angles to zero and H_N to a finite small value. Further analyses were performed setting $\theta = 0°$, and show that, irrespective of the value employed for H_N, all curves overlap and recover the standard response of the basic single plane model of [4], in the absence of dilation.

4.1.2 Sensitivity to θ

Figure 7 shows the shear stress-slip and dilation-slip curves for $H_N = 0.025$ and θ varying between 0 and $45°$ with $\sigma_N = -0.2$ MPa and the other model parameters as in Table 1. Asperity degradation is again excluded in these examples so that $\theta = \theta_0 = \theta_f$.

In Figure 7(b) it is easier to appreciate that the dilation-slip curve starts with a negative slope and a small initial part where dilation is negative. This is because, initially, dilation is negative due to the interface compliance under the applied compressive stress. Positive dilation is then found for larger vaues of the prescribed slip.

It is also worth noting that when θ increases from 18° to 45° there is a significant difference in the shear stress-slip curve whereas there is little change in the dilation response.

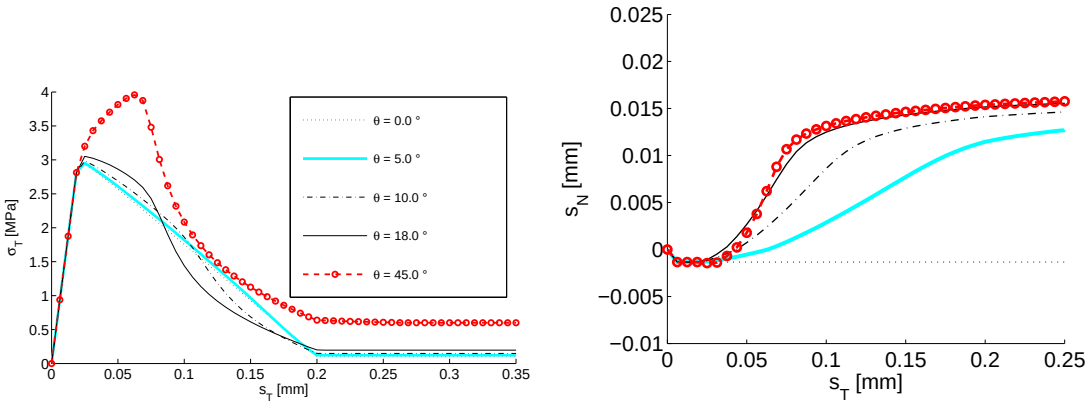

Figure 7: Response obtained for monotonically increasing slip, constant $\sigma_N = -0.2$ MPa , $H_N = 0.025$ and varying θ: (a) shear stress vs. slip ($\sigma_T - s_T$); (b) dilation vs. slip ($s_N - s_T$).

4.1.3 Sensitivity to η

Parameter η controls the initial elastic interface stiffness according to relation (9), so that the closer to unity is η, the stiffer the interface, with infinite stiffness reached in the limit of $\eta = 1$.

Figures 8(a) and 8(b) respectively show the shear-slip and the dilation-slip curves for different values of η ranging from 0.7 to 0.999, for $\theta = \theta_0 = \theta_f = 25°$, $H_N = 0.5$, $\sigma_N = -0.2$ MPa and all the other material parameters as in Table 1. The figure shows that dilation asymptotically approaches H_N in the limit of an infinitely stiff interface ($\eta = 1$).

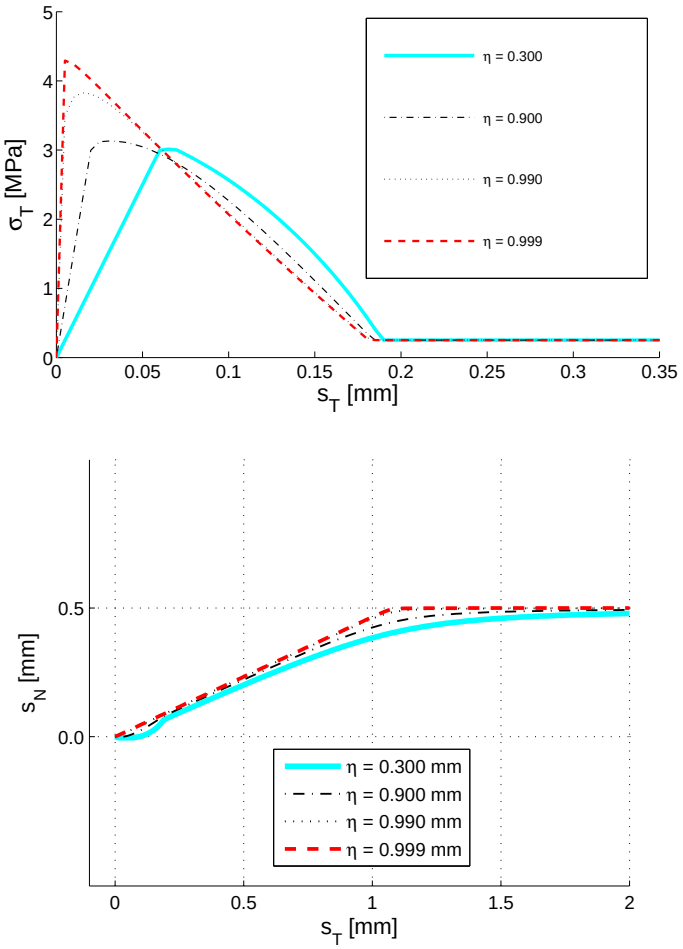

Figure 8: Response obtained for monotonically increasing slip, constant $\sigma_N = -0.2$ MPa , $H_N = 0.5$ and varying η: (a) shear stress vs. slip ($\sigma_T - s_T$); (b) dilation vs. slip ($s_N - s_T$).

4.1.4 Sensitivity to θ_0, θ_f and ζ_0

A second group of sensitivity analyses has been carried out to assess the dependency of the interface model to the initial microplane angle θ_0, the (asymptotic) final angle θ_f and the characteristic energy value ζ_0 controlling the rate of the asperity wear in accordance with Equation (22).

Table 2 reports the constitutive parameters kept fixed in these analyses. Notice that $\bar{G}_c$ is set equal to a negligible value to separate the role of cohesion from that played by the inclination angle, which physically reproduces the case of a pre-fractured interface.

Figure 9 shows the shear stress-slip and dilation-slip curves obtained, under constant

σ_{0n} [MPa]	σ_{0t} [MPa]	$\bar{G}_c$ [kJ/m^2]	η [–]	μ [–]
0.025	0.025	0.0005	0.99	0.5

Table 2: Material parameters employed in the analyses of the sensitivity to asperity degradation.

confinement pressure, $\sigma_N = -0.2$ MPa, for $\zeta_0 = 20$ kJ/m^2, $\theta_f = 7°$, $H_N = 5$ mm and θ_0 varying between $15°$ and $50°$.

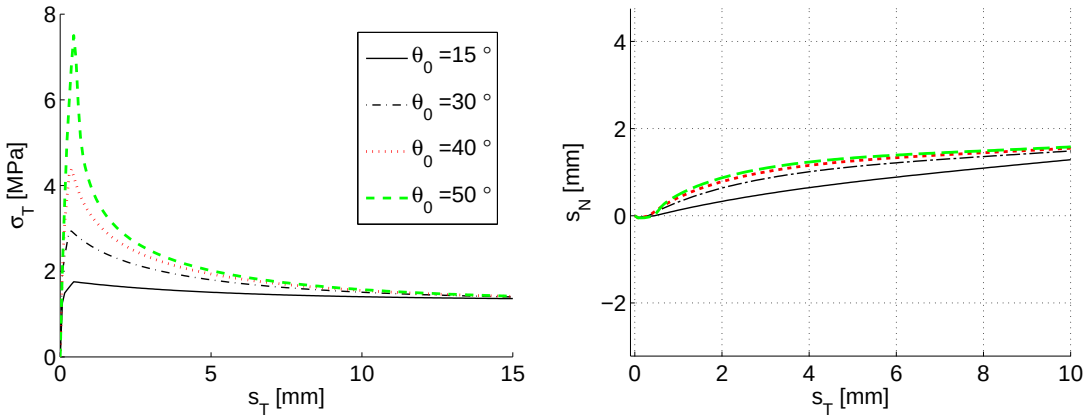

Figure 9: Response for monotonically increasing slip, for $\sigma_N = -2$ MPa, $\zeta_0 = 20$ kJ/m^2, $\theta_f = 7°$, $H_N = 5$ mm and θ_0 varying between $15°$ and $50°$: (a) shear stress vs slip; (b) dilation vs. slip.

In Figure 10 the initial asperity angle is kept fixed to $\theta_0 = 30°$ while θ_f is swept between $0°$ and $30°$. The other model parameters are $\zeta_0 = 20$ kJ/m^2, $\sigma_N = -2$ MPa and $H_N = 1$ mm.

It is interesting to observe that, as expected, the shear stress-slip curve obtained for $\theta_f = \theta_0 = 30°$ recovers a horizontal inelastic branch while, for $\theta_f = 0$, dilation asymptotically tends to zero. This last condition is suitable to model interfaces subjected to complete crushing and abrasion of asperities.

The sensitivity of the response to ζ_0, which is closely related to asperity toughness and geometry, is shown by the results in Figure 11, obtained for $\theta_0 = 30°$, $\theta_f = 7°$, $\sigma_N = -2$ MPa, $H_N = 2$ mm and ζ_0 varying.

Figure 11 reveals that by increasing ζ_0 from 1 to 10^4 kJ/m^2 the slip at complete asperity degradation changes from the range of millimeters to the range of centimeters.

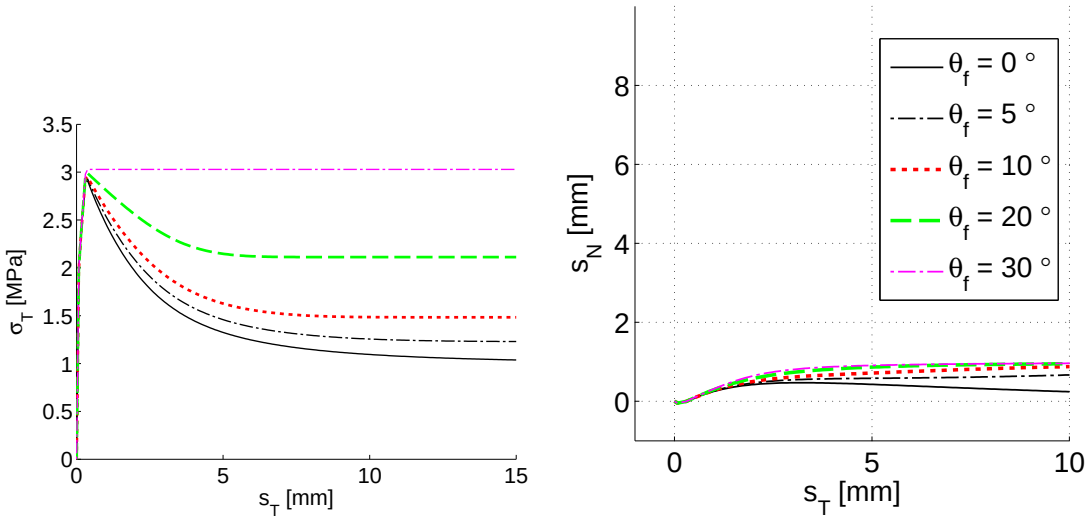

Figure 10: Response for monotonically increasing slip, for $\sigma_N = -2$ MPa, $H_N = 1$ mm, $\theta_0 = 30°$, $\zeta_0 = 20$ kJ/m^2 and θ_f varying: (a) shear stress vs. slip curves; (b) dilation vs. slip.

The value assigned to ζ_0, for a given interface, can be calibrated according to the size and toughness of the asperities. For instance, in Subsection 4.1.5 ζ_0 is calibrated accounting for the asperities present in granite rock pre-cracked joints, while in Section 4.2 this energy parameter is calibrated on account of the experimentally observed bond-slip curves where asperity degradation is due to crushing and shearing of concrete between the ribs.

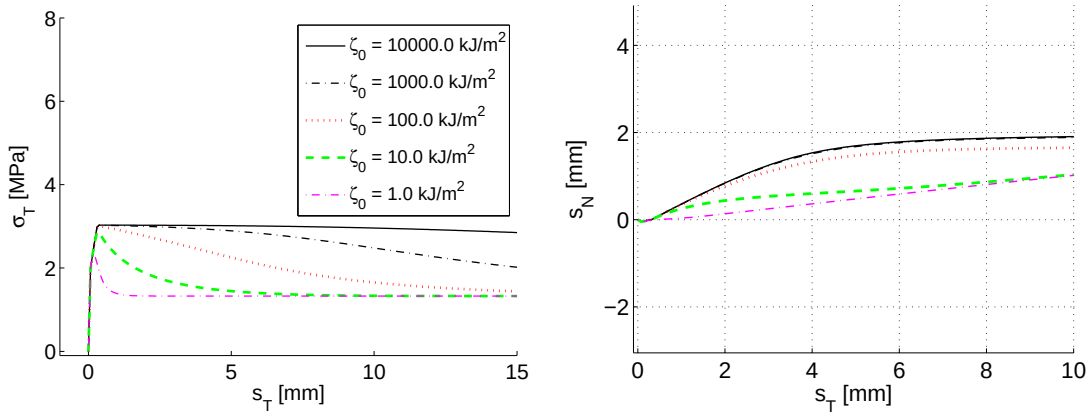

Figure 11: Response for monotonically increasing slip, $\theta_0 = 30°$, $\theta_f = 7°$, $\sigma_N = -2$ MPa, $H_N = 2$ mm and ζ_0 varying: (a) shear stress vs slip; (b) dilation vs slip.

4.1.5 Single-point behavior under cyclic response with asperity degradation

The single-point behavior under cyclic response is analyzed in this next group of examples, in presence of asperity degradation. Firstly, a typical cyclic response obtained with the proposed model is shown in Figures 12a-12c for a cyclic slip history, with $H_N = 5.0$ mm, $\zeta_0 = 20.0$ kJ/m^2 and the remaining parameters equal to those of the previous example of Figure 11.

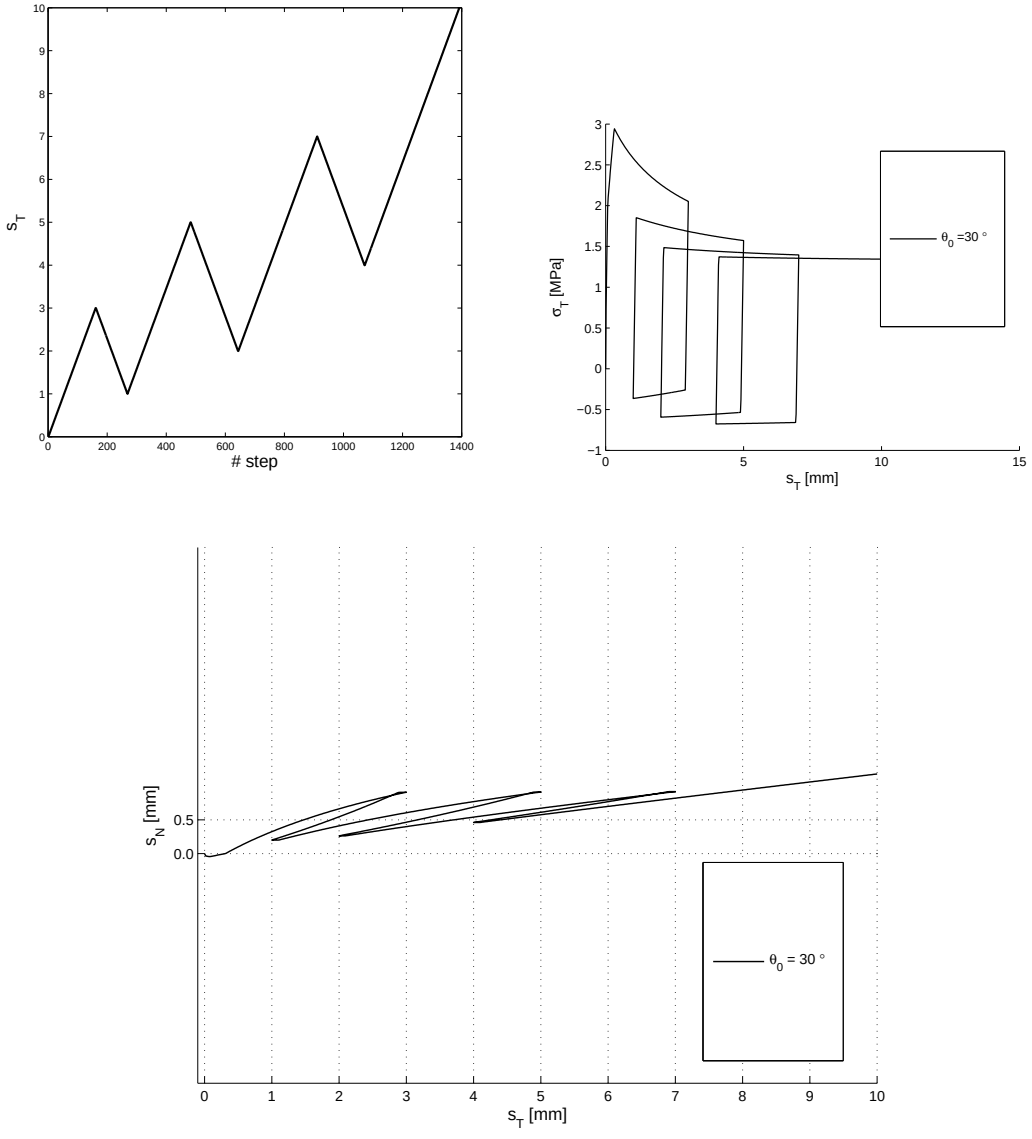

Figure 12: Responses under cyclic loading with the model parameters as in the case of Figure 11: (a) prescribed slip history; (b) shear stress response and (c) dilation response.

Next the predictive capabilities of the single-point response are validated against the experimental results for the granite joints tested by Lee et al. [12], for which material parameters used in the simulations are calibrated as follows:

1. Since all tested joints were pre-fractured, $\bar{G}_c$, σ_{0n} and σ_{0t} are set to negligible values.

2. Considering the relatively small sensitivity to η revealed in Figure 8 for $\eta > 0.9$ a value of $\eta = 0.99$ was taken.

3. The friction coefficient μ is taken equal to the value $\mu = 34.6°$ measured by Lee et al. [12] on smooth granite joints made by saw-cutting. The close correlation shown in Figure 13 between the experimental shear stress-slip curve under cyclic loading reported in [12] and the curve numerically obtained with our model with $\mu = 34.6°$ and $\theta = \theta_f = 0$ represents a first element of successful validation of the model in terms of simulation of friction.

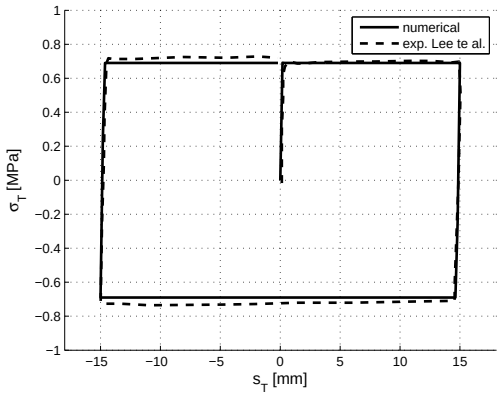

Figure 13: Comparison between the experimentally measured [12] and our numerically obtained shear stress-slip curves for smooth granite joints subject to cyclic testing.

4. Parameters H_N and θ_f are then calibrated by numerically curve fitting with the proposed model the shear stress-slip and dilation-slip curves experimentally obtained by Lee et al. [12] during the second cycle and reported in Figure 14(a) and 14(b), respectively, resulting in $H_N = 4$ mm and $\theta_f = 9°$.

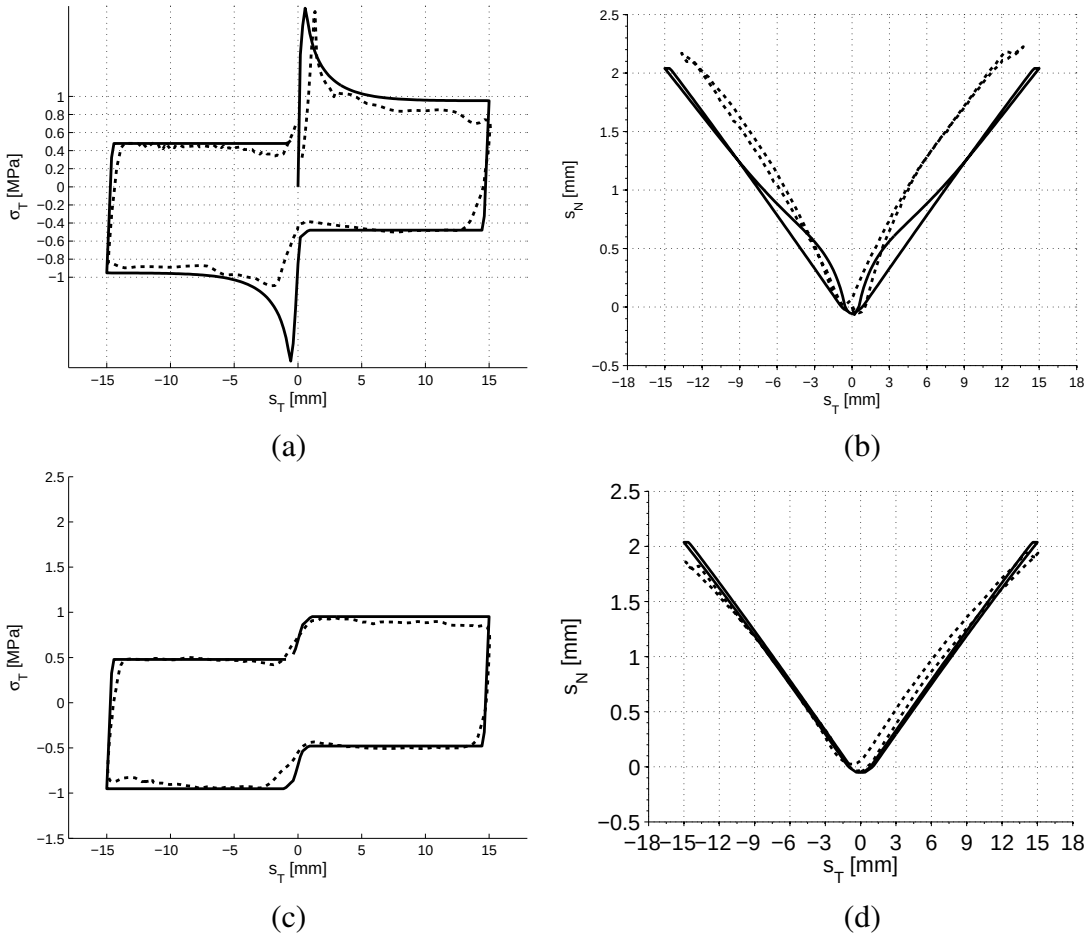

Figure 14: Experimental (dotted lines) and numerical (solid lines) shear stress-slip and dilation-slip curves for the rough granite joints tested by Lee et al. [12] during the first (a) and (b) and second (c) and (d) cycle.

5. Finally, θ_0 and ζ_0, are calibrated by curve fitting the shear stress-slip curves in Figures 14(a) and 14(b) relative to the first cycle, resulting in $\theta_0 = 30°$ and $\zeta_0 = 6.666$ N/mm.

Ultimately, a satisfactory correlation is obtained for all curves of Figure 14 with a single set of parameters, which provides a good validation for the proposed model in absence of initial cohesion. The only feature not adequately captured by the model response is the reduction in the initial stiffness at the beginning of the second half (i.e. during reverse loading) of the first loading cycle.

4.2 Pull-out test of a steel bar from a concrete block

In this subsection the interface model is employed in a structural analysis to simulate the pull-out test of a ribbed steel bar from a cylindrical concrete specimen carried out by Shima et al. [28]. This test is selected as a benchmark among many pull-out tests documented in the literature essentially for two reasons. Firstly, the geometrical regularity of the ribs employed in these experiments and their axial-symmetry well fits the geometrical assumptions of the model. Secondly, the relatively large dimensions of the concrete specimen, as well as the insertion of a clay sleeve with very small adherence in an initial part at the loaded end of the steel bar, prevents the formation of splitting cracks and results in negligible concrete damage or plasticity, except in a thin region immediately adjacent to the steel bar and its ribs.

The pull-out test has been simulated in an axial-simmetric finite-element analysis with the code ABAQUS [11] modelling the response of such thin region with the proposed cohesive model, which was implemented as a user-subroutine (UMAT).

4.2.1 Test set-up

The experimental apparatus is schematized in Figure 15. A SD30-steel bar of diameter $D = 19.5$ mm is placed at center axis of a cylindrical concrete block. An initial $10D$-long (195 mm) region with weakened bond is created in the vicinity of the loaded end of the bar, by inserting a clay sleeve surrounding the bar, in order to avoid concrete damage and splitting at the top end of the concrete block. Below this region the steel-concrete bond is full. The load has been quasi-statically applied by prescribing the displacement of the top end of the bar up to a maximum value of 5.2 mm. The primary measured quantities are the top-end bar displacement, the pull-out force and the strain along the bar. The latter has been measured using pairs of 5 mm strain gauges, each pair placed diametrically opposite to each other and, along the bar, regularly spaced with a distance of 49 mm between each pair.

The nonlinear response during the test is the concurrent result of two different dam-

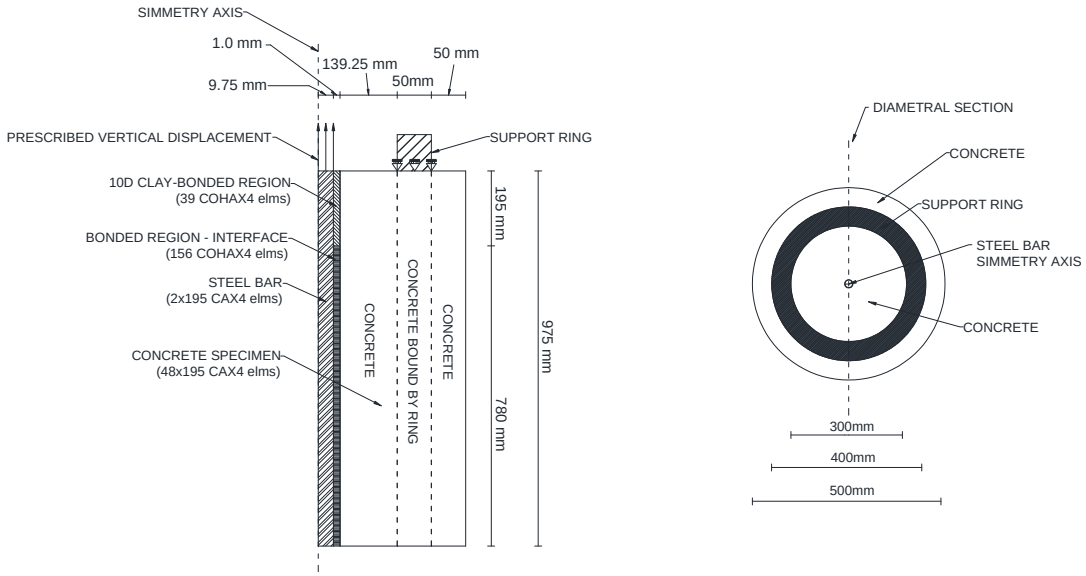

Figure 15: Experimental set-up [28].

age mechanisms. The first is the loss of cohesion, followed by contact loss, between the bar and the surrounding material, originated by the transverse restriction in the bar, due to longitudinal deformation and yielding. A second damage mechanism is the local wear and crushing of asperities in close proximity of the bar ribs.

Both these phenomena predominantly take place at the upper clay-bar interface where the bar yields and where slip is one order of magnitude larger than in the lower part of the bar, where concrete is subjected to much lower slip and the bar remains in the elastic range.

4.2.2 Finite-element model

A two-dimensional axial-symmetric finite-element model has been used for the simulation. A structured mesh of 4-noded fully-integrated axial-symmetric elements (named CAX4 in ABAQUS) is used for the steel bar and the concrete block with an element size of approximatively 5×5 mm^2. On the clay-bar and concrete-bar interfaces, 4-noded axial-symmetric interface elements (named COHAX4 in ABAQUS), with approximate

element size of 5 mm, have been used. Details on the number of elements are reported in Figure 15.

For concrete, a linear elastic material model is employed in consideration of the negligible damage and plasticity found in the experiments. For the steel bar a small-strain von Mises elasto-plastic material model with nonlinear isotropic hardening has been used, in order to reproduce the significant excursion in the plastic range of the bar in proximity of the loaded end.

The concrete and steel material properties used in the simulation are based on the data on these materials given in [28] and are reported in Tables 3 and 4. In particular, the Young's modulus, E_c, and Poisson's ratio, ν_c, of concrete were obtained using the correlations suggested by the Italian code of practice [1], considering an average cylinder strength f_c of 19.6 MPa [28]. For steel, the Young's modulus, E_s, the Poisson's ratio, ν_s, the first yield strength, f_y, and the total strain corresponding to the onset of hardening after the initial plastic plateau, ε_h, are reported in [28]. The complete isotropic-hardening curve reported in Table 4, relating the hardened yield strength σ_y to the equivalent plastic strain ε^p_{eq} is taken from the uni-axial stress-strain curve reported in [28].

E_c [GPa]	ν_c [-]	E_s [GPa]	ν_s [-]	f_{sy} [MPa]	ε_h [-]
2.621	0.2	190.0	0.3	350	0.0165

Table 3: Material properties employed for concrete and steel.

σ_y [MPa]	350	350	360	390	400	410
ε^p_{eq} [-]	0.0	0.0146	0.0164	0.0206	0.0224	0.0242
σ_y [MPa]	415	427	433	444	450	460
ε^p_{eq} [-]	0.026	0.0278	0.0292	0.0314	0.0352	0.038

Table 4: Representative hardened yield strength values vs corresponding equivalent plastic strain values in the isotropic-hardening curve.

To reproduce the local interface response at the concrete-bar cohesive zone and at the clay-bar cohesive zone, the present model has been used employing for these two

cylindrical surfaces different mechanical parameters to account for the significantly different asperity geometry and damage evolution determined by the different mechanical properties of clay and concrete.

The following rationale was used to calibrate the model parameters on both the clay-bar and the concrete-bar interfaces. In agreement with [26] the following conditions are set $\sigma_{0n} = \sigma_{0t} = \sigma_0$. For both interfaces η has been taken equal to 0.995 to obtain an interface stiffness high enough to well simulate the initial undamaged response, yet avoiding ill-conditioning. Furthermore, in this range the sensitivity of the structural response obtained to η was found to be negligible, in agreement with [2, 27].

To account of the much larger scratch resistance of steel, compared to concrete and clay, for both interfaces θ_f was set to 0 degrees. Physically this can be interpreted as assuming that the asperities in concrete and clay can be almost or completely smoothened at full asperities degradation.

For the concrete-bar interface, based on the data on the geometry of the bar ribs reported in [29], the values $\theta_0 = 45^\circ$ and $H_N = 1.5$ mm were set.

Numerical sensitivity analyses have revealed a predominant influence of the clay-bar interface parameters on the overall response and a less pronounced influence of the parameters of the concrete-bar interface located in the interior region. This influence is expected, since the clay-bar region is next to the loaded end and since this zone is weaker. However, since no data on the clay material properties are provided in [29], the remaining parameters were determined by curve fitting the primary data reported [29], namely (i) the pull-out stress vs top-end displacement-to-diameter ratio and (ii) the point-wise strain profiles measured by the strain gauges placed along the bar. These experimental data are reported in Figure 16 (dotted curve) and 17 (markers), respectively.

For the clay-bar interface, curve-fitting of the first branch of the load-displacement curve in Figure 16, corresponding to a displacement-to-diameter ratio, s/ϕ, up to a value of 0.05, provided $\sigma_0 = 0.5$ MPa and $\bar{G}_c = 0.05$ N/mm.

The remaining parameters were determined by curve fitting the experimental points

in Figure 17 and the second part of the curve in Figure 16, corresponding to a ratio s/ϕ in the range $[0.05,\ 0.4]$. The resulting parameters are collected in Table 5.

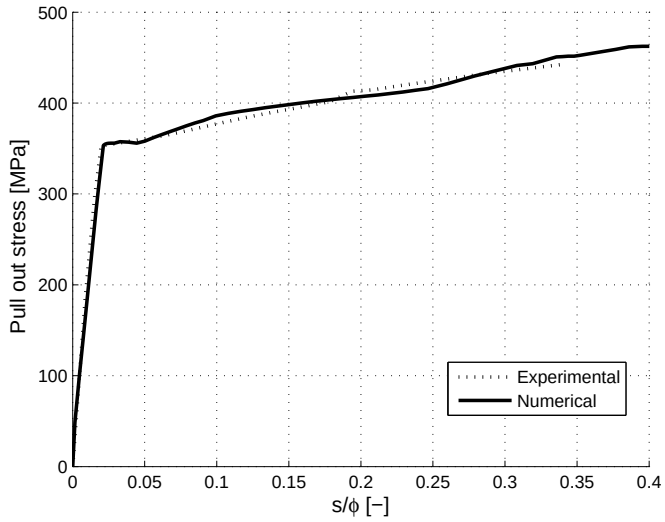

Figure 16: Numerical-experimental comparison. Pull-out stress plotted versus the ratio of the applied displacement at the loaded end to the diameter.

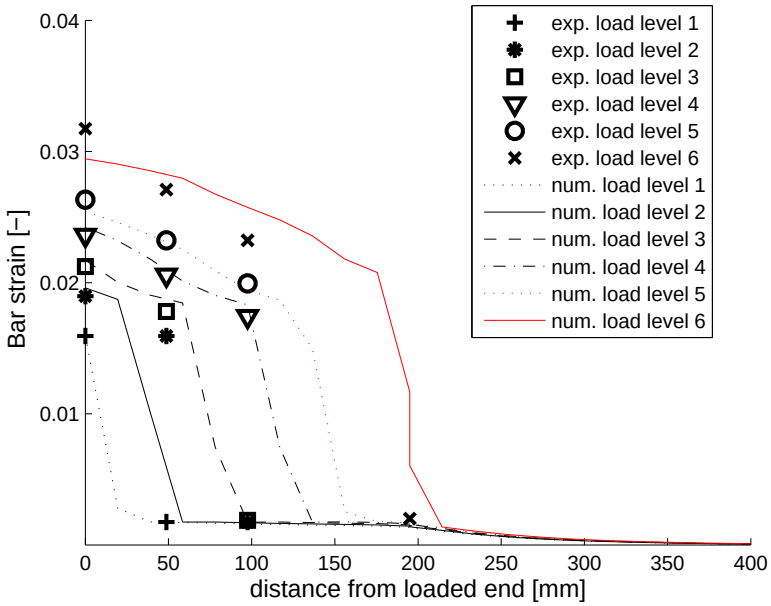

Figure 17: Comparison of measured axial strain (markers) and computed bar axial strain (lines) for different loading levels.

Figures 16 and 17 show overall good overall correlation between numerically predicted and experimentally measured data. These results in conjunction with the good

	σ_{0n}=σ_{0t}	$\bar{G}_{cn} = \bar{G}_{ct}$	η	μ	θ_0	θ_f	H_N	ζ_0
	[MPa]	[N/mm]	[-]	[-]	[deg.]	[deg.]	[mm]	[N/mm]
Concrete-bar	1.0	0.1	0.995	0.7	45.0	0.0	1.5	33.3
Clay-bar	0.5	0.05	0.995	0.6	1.75	0.0	0.5	33.3

Table 5: Concrete-bar and clay-bar interface material parameters.

correlation obtained for the pre-cracked granite joints, can be considered as an overall successful validation for the proposed model.

5 Conclusions

A new cohesive-zone model, in which de-cohesion, friction, dilation and surface wear are captured with simplified, yet effective micro-mechanical assumptions within a two-scale formulation, has been presented, discussed and validated. With respect to previous work, which this development build on, the possibility of accounting for the finite depth of the surface asperities and for their progressive wear and rupture have been introduced in the model and an extensive numerical investigation has been presented to demonstrate the validity of the proposed approach.

The effectiveness of the proposed model lies in two main features: (i) the model requires the identification of a relatively small number of parameters; (b) each of these parameters has a very clear physical meaning, which also makes it easier to identify them with solid engineering arguments, such as those used in the applications presented in this paper; (c) the model captures the essential processes that contribute to the energy dissipation during crack initiation and propagation in cases where plasticity, visco-plasticity, visco-elasticity and crack branching are negligible.

To demonstrate the effectiveness of the proposed model the results of a number of numerical simulations were described and discussed in detail. A sensitivity analysis of the model to the key parameters describing the surface geometry at the micro-scale and its evolution as a result of wear and rupture of the asperities has first been documented.

A validation of the single-point response predicted by the model, in absence of initial

cohesion, against the experimental results by [12] was then reported. The calibration procedure used to identify the model parameters in this case was described in detail and discussed.

Finally, the capability of the model to provide accurate predictions of structural problems including interfaces with initial cohesion is assessed by simulating the pull-out test of a mild-steel bar from a concrete cylindrical block made and reported by Shima et al. [28]. Again, the rationale used to identify the model parameters is explained in detail.

While the model is of course not able to capture all the complex damage processes occurring at the micromechanical scale, the numerical results demonstrate that it captures all the qualitative aspects of the dissipative processes simulated, with a quantitative accuracy that appears satisfactory, also considering the overall uncertainty that affects some of the experimental measures during the test.

The good compromise between sound physical foundations and richness of the response, on the one hand, and the limited number of parameters and their clear physical meaning, on the other hand, suggest that the proposed model has high potential to be employed as an effective and versatile tool in many engineering problems.

Further research aiming to increase the applicability, accuracy and robustness of the model should address a number of points. While the simplicity of the micromechanical assumptions, and in particular of the RIA used here, are an advantage as discussed above, the possibility of enriching the model with additional details such as a statistical distribution of the depth of the asperities and inclination of microplanes is probably one of the first points worth to be addressed. Furthermore, for more systematic applications to real-life and industrial problems, research work is needed to devise standard, and most likely problem-dependent, testing procedures for the identification of the model parameters. The extension to three-dimensional cases is another important aspect which requires future efforts.

References

[1] NTC2008 - Nuove Norme Tecniche per le Costruzioni, No. 30, 2008.

[2] G. Alfano, M. Crisfield, Finite element interface models for the delamination analysis of laminated composites: mechanical and computational issues, International Journal for Numerical Methods in Engineering 50 (7) (2001) 1701–1736.

[3] G. Alfano, S. Marfia, E. Sacco, A cohesive damage-friction interface model accounting for water pressure on crack propagation, Computer Methods in Applied Mechanics and Engineering 196 (1-3) (2006) 192 – 209.

[4] G. Alfano, E. Sacco, Combining interface damage and friction in a cohesive-zone model, International Journal for Numerical Methods in Engineering 68 (5) (2006) 542–582.

[5] D. Aubry, A. Modaressi, H. Modaressi, A constitutive model for cyclic behaviour of interfaces with variable dilatancy, Computers and Geotechnics 9 (1-2) (1990) 47 – 58, special Issue on Soil-Structure Interaction.

[6] N. Barton, V. Choubey, The shear strength of rock joints in theory and practice, Rock mechanics 10 (1-2) (1977) 1–54.

[7] S. Brown, C. Scholz, Broad bandwidth study of the topography of natural rock surfaces, Journal of Geophysical Research: Solid Earth (1978–2012) 90 (B14) (1985) 12575–12582.

[8] M. Frémond, Adhérence des solides, Journal de Mécanique Théorique et Appliquée 6 (3) (1987) 383–407.

[9] R. Goodman, J. Dubois, Duplication of dilatancy in analysis of jointed rocks, Journal of the Soil Mechanics and Foundations Division 98 (4) (1972) 399–422.

[10] D. Helgeson, A. Aydin, Characteristics of joint propagation across layer interfaces in sedimentary rocks, Journal of Structural Geology 13 (8) (1991) 897 – 911.

[11] Hibbitt, Karlsson, Sorensen, ABAQUS: Theory Manual, Hibbitt, Karlsson and Sorensen, 1997.

[12] H. Lee, Y. Park, T. Cho, K. You, Influence of asperity degradation on the mechanical behavior of rough rock joints under cyclic shear loading, International Journal of Rock Mechanics and Mining Sciences 38 (7) (2001) 967–980.

[13] I. Mihai, A. Jefferson, A multi-asperity plastic-contact crack plane model for geomaterials, International Journal for Numerical and Analytical Methods in Geomechanics 37 (11) (2013) 1492–1509.

[14] Z. Mroz, G. Giambanco, An interface model for analysis of deformation behaviour of discontinuities, International Journal for Numerical and Analytical Methods in Geomechanics 20 (1) (1996) 1–33.

[15] M. Musto, G. Alfano, A novel rate-dependent cohesive-zone model combining damage and visco-elasticity, Computers & Structures 118 (2013) 126–133.

[16] D. Oliveira, P. Lourenço, Implementation and validation of a constitutive model for the cyclic behaviour of interface elements, Computers & Structures 82 (17-19) (2004) 1451 – 1461.

[17] H. Parland, Stability of rigid body assemblages with dilatant interfacial contact sliding, International Journal of Solids and Structures 32 (2) (1995) 203 – 234.

[18] M. Plesha, Constitutive models for rock discontinuities with dilatancy and surface degradation, International Journal for Numerical and Analytical Methods in Geomechanics 11 (4) (1987) 345–362.

[19] S. Rafsanjani, P. Lourenço, N. Peixinho, Dynamic interface model for masonry walls subjected to high strain rate out-of-plane loads, International Journal of Impact Engineering 76 (2015) 28–37.

[20] M. Raous, Interface models coupling adhesion and friction, Comptes Rendus Mécanique 339 (7-8) (2011) 491 – 501, surface mechanics : facts and numerical models.

[21] M. Raous, L. Cangémi, M. Cocu, A consistent model coupling adhesion, friction, and unilateral contact, Computer Methods in Applied Mechanics and Engineering 177 (3-4) (1999) 383 – 399.

[22] A. Rekik, F. Lebon, Homogenization methods for interface modeling in damaged masonry, Advances in Engineering Software 46 (1) (2012) 35 – 42.

[23] B. Schott, H. Schmeling, Delamination and detachment of a lithospheric root, Tectonophysics 296 (3-4) (1998) 225 – 247.

[24] J. Segurado, J. LLorca, A computational micromechanics study of the effect of interface decohesion on the mechanical behavior of composites, Acta Materialia 53 (18) (2005) 4931 – 4942.

[25] R. Serpieri, G. Alfano, Bond-slip analysis via a thermodynamically consistent interface model combining interlocking, damage and friction, International Journal for Numerical Methods in Engineering 85 (2) (2011) 164–186.

[26] R. Serpieri, E. Sacco, G. Alfano, A thermodynamically consistent derivation of a frictional-damage cohesive-zone model with different mode i and mode {II} fracture energies, European Journal of Mechanics - A/Solids 49 (2015) 13 – 25.

[27] R. Serpieri, L. Varricchio, E. Sacco, G. Alfano, Bond-slip analysis via a cohesive-zone model simulating damage, friction and interlocking, Fracture and Structural Integrity (29) (2014) 284–292.

[28] H. Shima, L. Chou, H. Okamura, Bond characteristics in post-yield range of deformed bars, Concrete Library of the Japan Society of Civil Engineers 10 (1987) 113–124.

[29] H. Shima, L. Chou, H. Okamura, Micro and macro models for bond in reinforced concrete, Journal of the Faculty of Engineering 39 (2) (1987) 133–194.

[30] L. Snozzi, J. Molinari, A cohesive element model for mixed mode loading with frictional contact capability, International Journal for Numerical Methods in Engineering 93 (5) (2013) 510–526.

[31] M. Snyman, J. Martin, A consistent formulation of a dilatant interface element, International Journal for Numerical and Analytical Methods in Geomechanics 16 (7) (1992) 493–527.

[32] A. Spada, G. Giambanco, P. Rizzo, Damage and plasticity at the interfaces in composite materials and structures, Computer Methods in Applied Mechanics and Engineering 198 (49-52) (2009) 3884 – 3901.

[33] S. Stupkiewicz, Fiber sliding model accounting for interfacial micro-dilatancy, Mechanics of Materials 22 (1) (1996) 65 – 84.

[34] S. Stupkiewicz, Z. Mróz, Modeling of friction and dilatancy effects at brittle interfaces for monotonic and cyclic loading, Journal of Theoretical and Applied Mechanics 39 (2001) 707–739.

[35] J. Toti, S. Marfia, E. Sacco, Coupled body-interface nonlocal damage model for {FRP} detachment, Computer Methods in Applied Mechanics and Engineering 260 (2013) 1 – 23.

[36] Y. Yan, T. Sumigawa, L. Guo, T. Kitamura, Strength evaluation of a selected interface in multi-layered nano-material, Engineering Fracture Mechanics 116 (2014) 204 – 212.

[37] S. Zlotnik, P. Díez, M. Fernández, J. Vergés, Numerical modelling of tectonic plates subduction using x-fem, Computer Methods in Applied Mechanics and Engineering 196 (41-44) (2007) 4283 – 4293.